Crater formation caused by nanoparticle impact: A molecular dynamics study of crater volume and shape

Christian Anders,[1] Eduardo M. Bringa,[2,3] Fabricio D. Fioretti,[2] Gerolf Ziegenhain,[1] and Herbert M. Urbassek[1,*]

[1]*Physics Department and Research Center OPTIMAS, University Kaiserslautern, Erwin-Schrödinger-Straße, D-67663 Kaiserslautern, Germany*

[2]*Instituto de Ciencias Básicas, Universidad Nacional de Cuyo, Mendoza, 5500 Argentina*

[3]*CONICET, Mendoza, 5500 Argentina*

(Received 8 March 2012; revised manuscript received 22 May 2012; published 20 June 2012)

We present molecular-dynamics simulations of cratering induced by projectiles containing $N \cong 10$–10^6 atoms in the velocity regime of 1–70 km/s. Self-bombardment of a condensed Ar and a Cu target are studied. We corroborate the earlier finding that for small clusters, $N \lesssim 1000$, above a threshold regime, the crater volume scales linearly with the total impact energy E; by scaling energies to the target cohesive energy U, crater volumes of such diverse materials as condensed Ar and Cu coincide. At threshold $E_{\rm th}$, craters are shallow. They become hemispheric at energies $\sim 5E_{\rm th}$. Part of the material excavated from the crater is sputtered. This fraction decreases with cluster size N. Relatively less material is sputtered from an Ar target than from a Cu target. Larger cluster impact, which we simulate up to $N = 3 \times 10^6$, shows a stronger size effect, such that the resulting craters increase slightly more than linearly with total energy. This finding is discussed in light of available experimental data for μm- and mm-sized projectiles. Simulations on ductile samples containing pre-existing defects (nanocracks) show that such pre-existing damage plays a negligible role for crater formation and size in metals.

DOI: 10.1103/PhysRevB.85.235440 PACS number(s): 79.20.Rf, 79.20.Ap, 61.80.Lj

I. INTRODUCTION

Impact of material surfaces by μm- and nm-sized hypervelocity projectiles is of considerable interest in space science, astrophysics, and planetary sciences.[1] The target materials may consist of rock or ice (atmosphereless planets, moons, asteroids, or comets), or of metals (spacecraft), while the projectiles of interest are dust grains (again composed of rock and ice), but also of metal and other debris in the low earth orbit environment. Dust grains may measure between 1 nm and 1 μm,[2] while debris may also have considerably larger sizes. Typical velocities involve 3–100 km/s; this is conventionally called the hypervelocity impact regime. It is often assumed to cover velocities beyond $\gtrsim$3 km/s,[3,4] where the projectile completely disintegrates upon impact. On an energy scale, the kinetic energy per atom of the projectile hence exceeds the cohesive energy of the projectile and often also the cohesive energy of the target material.

Several satellite missions have been used to investigate dust-materials interactions. Here, we mention the early Solar Maximum satellite[5] and the Long Duration Exposure Facility mission.[6,7] CASSINI explored the interaction of dust particles with metal targets in its Cosmic Dust Analyzer experiment;[8] STARDUST brought cometary dust particles home from comet Wild 2.[9] ROSETTA will explore the cometary dust of the comet Schurjumow-Gerasimenko. The space shuttle brought solar panels from the HUBBLE telescope down for investigation of cratering.[10] Due to the importance of these studies for space science, experimental research has been carried out in several laboratories.[7,11–14]

Cratering experiments are also performed using single heavy ions[15] or clusters containing of the order of $N = 1000$ atoms.[16] The crater shapes found resemble closely those of macroscopic impacts.

On the theoretical side, understanding was initially guided by setting up scaling relationships to correlate measured crater volumes with various experimental and materials parameters at macroscopic scales.[17–19] Later on, continuum (so-called hydrocode) simulations were performed to investigate the fate of the projectile and the bombarded target.[20–22] Such modeling requires a thorough understanding of the material response under extreme conditions of temperature, pressure, strain, and strain rate, going well beyond the usual knowledge of the (equilibrium) equation of state, and often using equilibrium shock data along the Hugoniot line to calibrate models.[23] Quite recently, another possibility for investigating cratering phenomena has been offered by the technique of molecular-dynamics simulations.[24–30] These are based on a knowledge of the interatomic interaction potential only, and thus require, in principle, less input for describing the materials behavior than hydrocode modeling.

While the simulation work up to around 2006 mainly considered small-cluster impacts,[31] more recently, interest in large-cluster impacts became dominant. Aoki *et al*. simulated the impact of Ar_{1000} clusters on Si surfaces and determined the evolution of the crater diameter and the sputter yield.[29] Samela and Nordlund[28,32] studied Au_N cluster impacts on Au, up to sizes of $N = 3 \times 10^5$, at a velocity of 22 km/s. They correlate their data on crater volumes V with cluster size N and total impact energy E using a law $V \propto NE^{1.65}$ taken from macroscopic crater scaling theory,[19] and assert that their data approach the macroscopic trend for cluster sizes $N \gtrsim 10^5$. These findings were later corroborated by simulations of equivelocity Ar cluster impact on silica.[30] Crater formation was also simulated for more complex targets; we mention the work by Delcorte and Garrison on crater formation induced by C_{60} impact in polymeric targets.[33] Recently, we showed[34] that the volume of cluster-induced craters scales proportional to the total impact energy, and that the craters induced in Cu and Ar have similar size when the impact energy is scaled to the target cohesive energy and the crater volume is measured in units

of the target atomic volume. These results were extended to impacts of clusters containing up to 7.4×10^6 atoms (diameter 55 nm), at the limit of today's computational facilities.[35] In that work, also the scaling of the crater formation time, the target strain rates and the maximum target pressures were explored, and the connection to macroscopic cratering experiments was established.

In this paper, we corroborate and extend our previous results by modeling impacts with projectiles containing $N = 10$–10^6 particles. By aiming at a systematic presentation of simulation data in terms of cluster size and impact energy, we describe the scaling of the resulting crater volumes on projectile energy and size. As novel aspects, we study the emission yields and the shape of the induced craters. Comparison to available experimental data, obtained for clusters containing $N = 10^{11}$–10^{21} atoms, allows us to discuss the similarities and the differences in the cratering induced by nm- and μm-sized projectiles.

II. METHOD

The molecular-dynamics (MD) method we employ is standard.[26,36] Results for two materials are presented: Ar and Cu. The bombarding clusters always consist of the same material as the irradiated target, i.e., only the case of self-bombardment is studied. Only perpendicular incidence is considered here. The clusters are of spherical shape and consist of N atoms. For the Ar system, a Lennard-Jones potential,[37,38] and for the Cu system, a many-body potential of the embedded-atom type,[39] have been employed.[40] In both cases, the potentials have been splined to an appropriate high-energy potential[41,42] in order to accurately model close collisions.

The Cu potential reproduces quite accurately the experimental behavior under shock conditions.[43] The Lennard-Jones potential produces a generic behavior under shock conditions similar to the one found in experiments for many materials.[44,45] The shear moduli of Cu and Ar given by these potentials are, respectively, 48 and 1.65 GPa,[46,47] and agree well with experimental values. The strength of the resulting crystals from MD simulations is $\sim G/50$, as expected from the large strain rates of the simulations and in agreement with recent experiments at similar strain rates.[48] The melting temperature of Cu and Ar at zero pressure given by the potentials used here are 1325 and 84 K.[49,50]

The bonding properties of the material are represented by the cohesive energy U, which amounts to $U = 3.54$ eV in the case of Cu and 0.082 eV for Ar. The total kinetic energy of the impacting cluster will be denoted by E. A scaled energy

$$\epsilon = E/U \tag{1}$$

may be introduced. For the convenience of the reader, we note that projectile speed v and specific energy E/N are connected by

$$v = 1.74\ [\mathrm{km/s}] \times \sqrt{\frac{E\ [\mathrm{eV}]}{N}} \tag{2}$$

for Cu projectiles, while the prefactor reads 2.19 for Ar.

The size of the target system varies between 10^4 and approximately 3×10^8 atoms, depending on the total cluster energy E. In order to study the cluster-induced crater sizes and shapes, the simulations have to be performed for sufficiently large times so that stable results are obtained; we employed simulation times up to $t_{\mathrm{end}} = 100$ ps, and occasionally longer. At the lateral and bottom sides of the simulation target, we use damped boundary conditions in order to mimic energy dissipation to the surrounding target material. The Cu target consists of an fcc crystal with (100) surface. In the case of Ar, we employ an amorphous target; test simulations showed no strong systematic differences between results for amorphous and crystalline targets. Of course, craters produced at lower energy tend to deviate slightly from hemispherical shape due to crystallographic effects in Cu, as seen in Fig. 1.

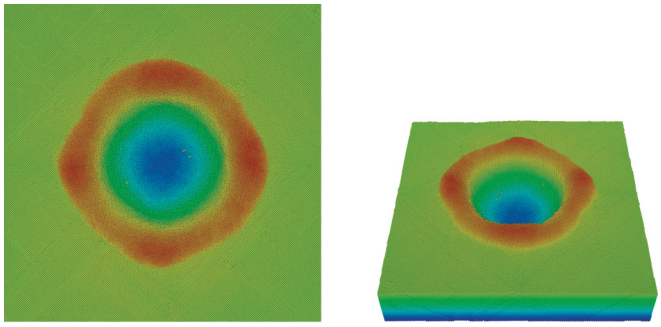

(a) (b)

FIG. 1. (Color online) Top (a) and perspective (b) view of Cu crater induced by impact of an $N = 10\,000$ atom Cu cluster at energy 50 eV/atom. Snapshots taken at 50 ps after impact. Color scale: height. Only the top fraction of the sample is shown.

We monitor the size and the shape of the bombardment-induced crater and verify that crater dimensions reach steady values at the end of the simulation time. For the large craters induced by the massive Cu clusters studied here, the following method has proven to be reliable to obtain crater sizes. The depth z of the crater is defined as the depression of the bombarded surface below the original surface at the point of cluster impact. A top view of the crater displays a rather circular shape in the original surface plane (cf. Fig. 1). Its radius is called r. A cross-sectional side view (cf. Fig. 2) shows that the craters can be well approximated by ellipsoids. We hence calculate the crater volume as the volume of a half-ellipsoid with axes r and z. In this paper, crater volumes

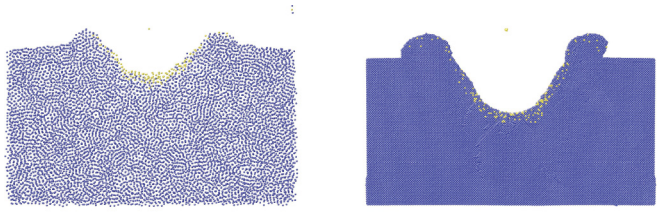

(a) (b)

FIG. 2. (Color online) Molecular-dynamics view on craters formed by cluster impact. Only a part of the simulation volumes is shown. Color differentiates projectile (yellow) and target (blue) atoms. (a) Crater formed at 30 ps after impact of an Ar_{1000} cluster at $E = 500$ eV, $E/NU \cong 6$, on an amorphous Ar target. (b) Cu crater induced by impact of an $N = 10\,000$ atom Cu cluster at energy 50 eV/atom, $E/NU \cong 14$. Snapshot taken at 100 ps after impact.

TABLE I. Simulation data on cratering induced by equivelocity Cu projectile impact on a Cu target.

N	v (km/s)	E/U	E/NU	r (Å)	z (Å)	r/z	V	V/N
57	5.47	1.59×10^2	2.79	0.4	0.04	10	8.4×10^{-4}	1.5×10^{-5}
612	5.47	1.70×10^3	2.79	9.5	1.8	5.3	2.9×10^1	4.7×10^{-2}
2809	5.47	7.82×10^3	2.79	34	13.6	2.5	2.79×10^3	9.9×10^{-1}
21 032	5.47	5.86×10^4	2.79	85	47	1.8	6.03×10^4	2.9×10^0
258 505	5.47	7.20×10^5	2.79	180	153	1.2	8.80×10^5	3.4×10^0
2 837 310	5.01	6.64×10^6	2.34	398	398	1.0	1.12×10^7	3.9×10^0

will be expressed as the equivalent number of missing target atoms, which is obtained with the help of the atomic volume of fcc Cu, $\Omega = 11.8$ Å^3 (and analogously 36.1 Å^3 for Ar) as

$$V = \frac{\frac{2}{3}\pi r^2 z}{\Omega}. \tag{3}$$

In the case of the weakly bonded Ar target, the material swells somewhat, even if no bombardment occurs. This happens even though we let the amorphized Ar target relax for 160 ps, before starting the simulation. We therefore perform a reference simulation of length t_{end} and take the resulting surface as the reference surface with respect to which we determine the crater volume. Crater depth z and radius r are determined as in the Cu target.

For small cluster sizes, and in particular for small cluster energies, the crater shape more strongly deviates from an ellipsoidal shape, and the method based on Ref. 24 defining the crater volume has been used in those cases. It consists in counting the number of the initially occupied lattice sites of the target, which are unoccupied after cluster impact.

For selected cases, we repeated our simulations with targets of increasing sizes and find always a similar behavior. Our results on crater volumes are unaffected within an error margin of generally $\pm 10\%$.

In the case of the Ar target, we study cluster sizes $N = 13$, 100, 1000 for reduced energies ϵ in the range from 1000 to 12 000. Here, five impacts were used for each cluster size and impact energy in order to obtain reliable averages. In the case of Cu clusters, sizes $N = 13$, 43, 100, 1000, and 10 000 were simulated. Additionally, a series of simulations with (almost) equivelocity impacts have been performed for cluster sizes $N = 57$ to $N \cong 3 \times 10^6$ (cf. Table I).

We note that cluster diameter D and particle number N are related by

$$D = 0.28\ [\text{nm}]\ \times N^{1/3} \tag{4}$$

for Cu projectiles, while the prefactor reads 0.41 for Ar. We note that both when measuring the crater size and shape we do not distinguish between projectile and target atoms since they consist of the same material. When studying cases where the projectile and target consist of different materials, one could study the shape of the implanted projectile cluster.

III. RESULTS

Figure 2 displays two cluster-induced craters as obtained from our simulations of a Cu and an Ar target for reduced energies $\epsilon/N \cong 10$. Note the qualitative similarity of the crater shapes even though the target materials are strongly different. Also, the craters look similar to those obtained in other molecular-dynamics simulations[24–27] and also to craters in experiments.[10,14]

A. Microscopic characteristics and temporal evolution of cratering

1. Argon

Figure 3 shows the dynamics induced by a 500-eV Ar_{1000} impact into an amorphous Ar target and the temporal evolution of the processes occurring in the target. After 3 ps, the projectile has just penetrated into the target and assumed a lenslike form; its upper side only sticks out slightly above the surface. Figures 3(b) and 3(c) display the extreme temperatures and pressures occurring in the target at a short time, 3 ps, after impact, when the crater has not yet started to form. Note that peak pressures are reached just below the impinging projectile [Fig. 3(b)]; at this time, the maximum temperatures are attained at the cluster-target interface, while the top of the projectile is still cold [Fig. 3(c)]. At 3 ps, the maximum pressure (1.6 GPa) is of the order of the bulk modulus of this material (2.75 GPa), and approaches the shear modulus (1.65 GPa).[47] The maximum temperatures reached (440 K) are considerably above the critical temperature of this material (150 K). We note that our temperatures and pressures are local values, averaged over volumes containing around 50 atoms. Local temperatures are evaluated in a comoving coordinate system, i.e., they do not include the flow motion of the material. Pressure includes both the virial contribution and the kinetic pressure.[52]

Figures 3(d) and 3(e) display the temporal evolution of the peak pressure and temperature in the target. Peak temperatures reach up to about 1000 K and are roughly stable within the first 3 ps after impact. Concomitantly, strong compressive pressures of more than 5 GPa are reached, albeit for somewhat shorter times, up to 2 ps. Note that this energetic phase, where exceedingly high temperatures and pressures are reached, lasts only up to around 6 ps; thereafter, these quantities have reached less extreme values of around 100 MPa and 100 K. Note the shoulder visible at 8–12 ps both in the pressure and temperature; only after this time, the target material can relax from the strong compression and heating imparted by the projectile momentum, and true target relaxation starts.

In Fig. 3(f), we characterize the compression state of the material by the strain in the target and projectile material experienced at the contact point between cluster and target. To be precise, for the projectile we compare the vertical diameter $s(t)$ with its initial diameter $s(0)$. For the target we use a cube of target material immediately under the impact point

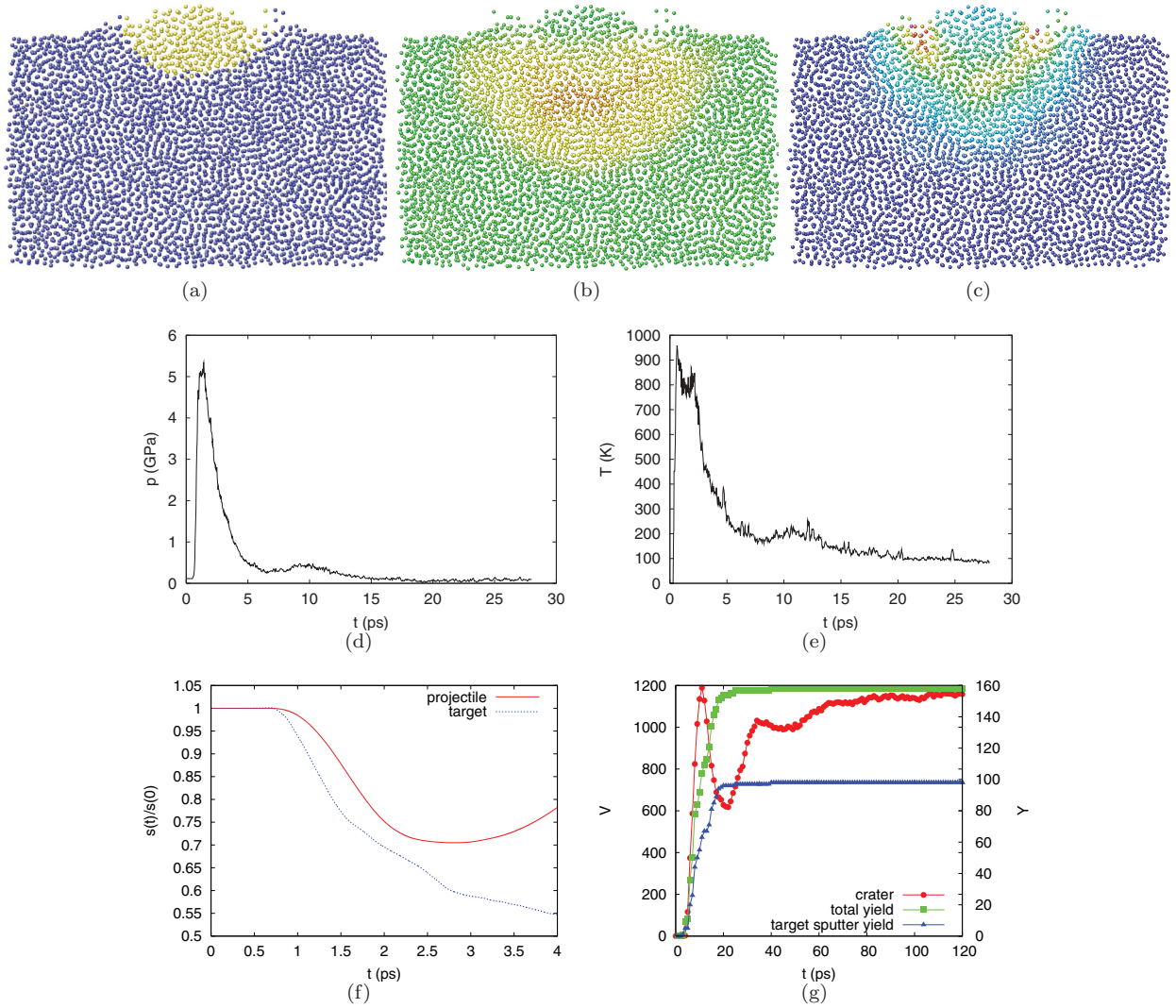

FIG. 3. (Color online) Various characteristics of $Ar_{1000} \rightarrow Ar$ impact at an energy of $E = 500$ eV. The shear modulus and critical temperature for Ar are 1.65 GPa and 150 K. (a) Snapshot showing penetration of projectile (yellow) into the target (blue) at $t = 3$ ps. (b) Pressure distribution in the target (162.5 Å wide) at $t = 3$ ps after impact. Green denotes zero pressure, while the highest pressure (orange) is compressive at 1.6 GPa. (c) Temperature distribution at $t = 3$ ps. The highest temperatures (red) reach 440 K. (d) Time dependence of maximum pressure p in the target. (e) Same for maximum temperature T. (f) Time dependence of relative deformation $s(t)/s(0)$ in the projectile and the target (see text). (g) Temporal evolution of crater volume V, total emission yield Y, and target sputter yield Y_s. An animation of this event is available as Supplemental Material.[51]

of the cluster with side length 14 Å. The data demonstrate a projectile compression of 30% and a target compression of 50%. The maximum projectile compression occurs at 1.2 ps after impact and precedes the maximum target compression. The decrease in strain for the projectile after 3 ps is due to its disintegration, as explained by Anders *et al.*[53]

Figure 3(g) monitors the time evolution of the crater volume V and of the emission yield Y. The latter quantity is defined as the number of (projectile or target) atoms which have been emitted. We can split it up into the sputter yield Y_s of target atoms and the reflection yield Y_r of reflected projectile atoms $Y = Y_s + Y_r$. To determine the emission yield, we first define the "substrate," which consists of all (projectile and target) atoms which have contact to the original target bottom; here, "contact" means that there exists a chain of atoms which are all bonded to each other in the sense that they are within the cutoff distance of the interatomic potential. Technically speaking, this is performed by using the clustering algorithm of Stoddard.[54] All atoms which do not belong to the substrate are called "emitted." The emission yield shows a simple monotonic increase between roughly 5 and 20 ps after impact, which also characterizes the sputter yield of target atoms. The total emission yield amounts to 158 atoms, of which 60 (38%) are reflected projectile atoms. The evolution of the crater volume is more complex. It reaches a first high maximum at around 10–12 ps after impact; note that this time coincides quite well with the shoulder in the temperature and pressure evolution shown in Figs. 3(d) and 3(e). Between 10 and 20 ps, the crater *shrinks* due to the rebound of the target; the strong compression of the target material below the crater relaxes and partly fills up the crater again. These oscillations continue until at around 100 ps, the crater volume

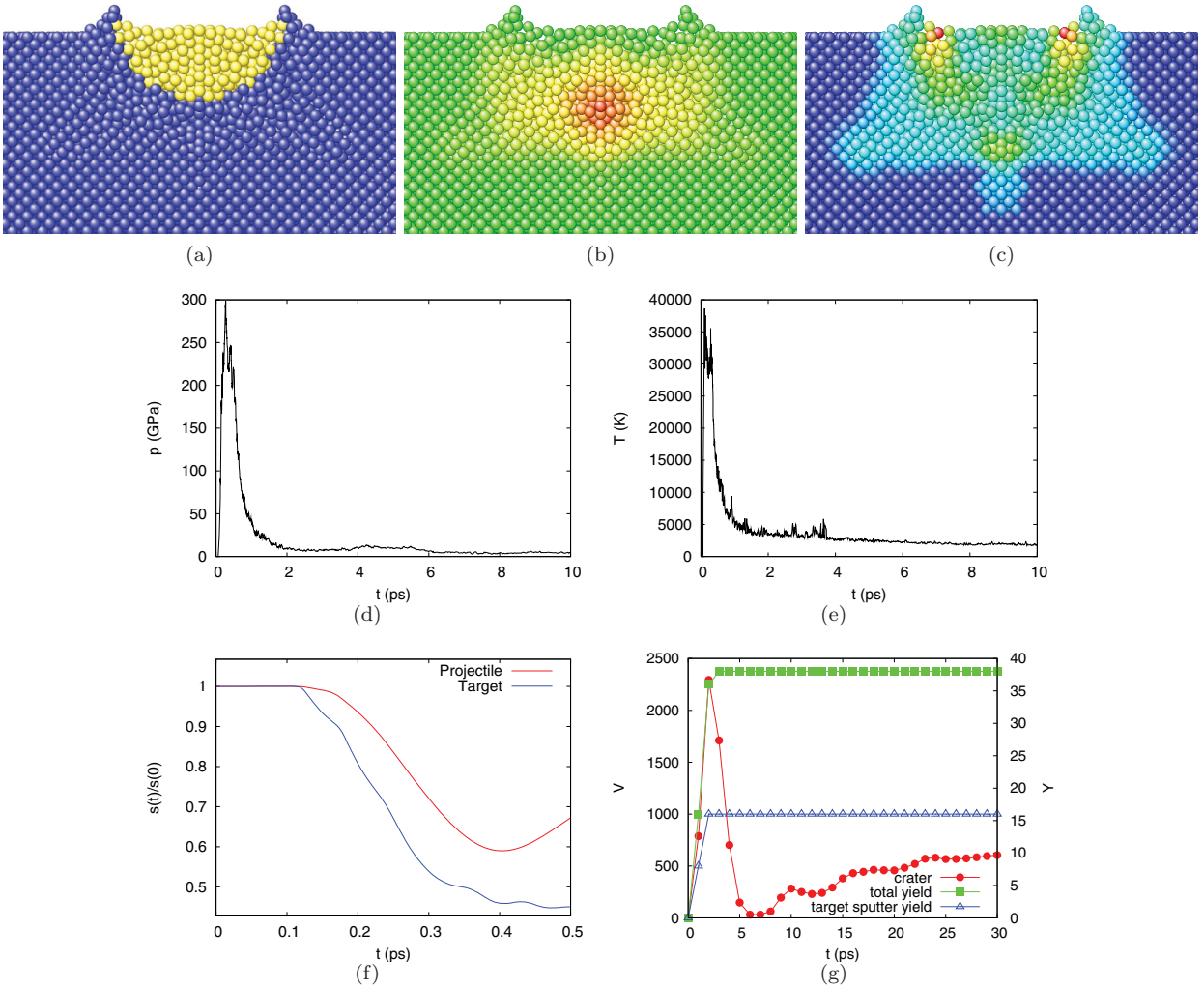

FIG. 4. (Color online) Various characteristics of $Cu_{1000} \rightarrow Cu$ impact at an energy of $E = 21.7$ keV. The shear modulus and critical temperature for Cu are 48 GPa and 7830 K. (a) Snapshot showing penetration of projectile (yellow) into the target (blue) $t = 0.47$ ps. (b) Pressure distribution in the target (94 Å wide) at $t = 0.47$ ps after impact. Green denotes zero pressure, while the highest pressure (orange) is compressive at 200 GPa. (c) Temperature distribution at $t = 0.47$ ps. The highest temperatures (red) reach 17 000 K. (d) Time dependence of maximum pressure p in the target. (e) Same for maximum temperature T. (f) Time dependence of relative deformation $s(t)/s(0)$ in the projectile and the target (see text). (g) Temporal evolution of crater volume V, total emission yield Y, and target sputter yield Y_s.

has stabilized. However, already after half this time, ∼50 ps, the crater volume can be determined within 10% accuracy. We note that the long duration and the strong nonmonotonicity of the crater evolution will occur most strongly in a softly bonded material like the case of Ar studied here.

Aoki *et al*. studied oscillations in radial crater size,[29] which are associated to crater opening and rim evolution. However, we are not aware of any previous results on the time evolution of the crater volume. A comparison of Figs. 3(d) and 3(e) with Fig. 3(g) shows that crater formation is governed by two quite distinct time scales: (i) a short time scale of around 3 ps, which rules projectile slowing down, and the formation of temperature and pressure peaks; (ii) the long time scale of 100 ps, which governs the crater formation, pressure and temperature relaxation, sputtering, and material transport at the crater walls and rims.

We repeated this simulation with targets of increasing sizes and find always a similar behavior. The position of the first maximum is connected to the size of the simulation volume, which points at an incomplete damping of the pressure wave emitted during cluster impact at the boundaries. However, the results on crater volumes are unaffected within an error margin of generally ±10%.

2. Copper

In Fig. 4, we show the analogous events for a $Cu_{1000} \rightarrow Cu$ impact at an energy of $E = 21.7$ keV. Note that the scaled energy $\epsilon/N = 6.1$ has been chosen identical as in the Ar_{1000} impact of Fig. 3. In order to compare the time scales, we note that projectile stopping is governed by the time t_0 it takes for the projectile to move a distance equal to its diameter D at the initial impact velocity v:

$$t_0 = D/v. \tag{5}$$

This time is $t_0 = 2.65$ ps for the Ar cluster of Fig. 3, but only 0.35 ps for the Cu cluster of Fig. 4. The pressure and

temperature snapshots have been taken at roughly this time to allow comparison. Note how [similar to Fig. 3(a)] the projectile has just penetrated the surface, and the crater rims are just being pushed upwards. The form of the projectile is hemispherical in this case. Note the good qualitative agreement between these distributions. These are also seen in the finer details, such as the fact that maximum temperatures occur for both impacts at the "friction" zone at the cluster's periphery close to the target surface; maximum pressures, on the other hand, are consistently observed immediately below the impactor. For the Cu target, the temperature profile is anisotropic due to the crystal anisotropy, but not for the amorphous Ar target.

The temporal evolution of the maximum pressure and temperature closely resemble those of the Ar target, if the scaling with the time scale t_0 [Eq. (5)] is taken into account. Note, however, that the maximum pressure $p_{\max}$ is considerably larger in Cu (250 GPa) than in Ar (5 GPa). In both cases, these values are around twice the respective bulk moduli, 138 for Cu and 2.75 GPa for Ar. Analogously, the maximum temperatures are much higher in Cu (>35 000 K) than in Ar (900 K). These values are more than four times above the critical temperatures (7830 and 150 K, respectively).[55,56] The relative deformations of both projectile and target show reasonable agreement. The projectile can be deformed to 60% of its original value (in the vertical direction) for Cu, and 70% for Ar. Since, however, the maximum deformation occurs roughly on the time scale of t_0 [Eq. (5)], and these differ by an order of magnitude, the maximum strain rates experienced are by a factor of around 10 different for the two materials. As discussed in detail in Ref. 53, the maximum strain rate η follow a law $\eta \propto v$, with a proportionality factor, which is only mildly dependent on the material (Ar or Cu), but depends like $N^{-1/3}$ on the cluster size.

The volume of the excavated crater assumes similar size, $V \cong 600$–1100, and also its temporal dependence is similar. Crater excavation starts at times $>t_0$; after reaching a high maximum, the crater apparently swings back due to the rebound of the compressed material below, until it saturates at around 100 ps (Ar) and 25 ps (Cu). We call this the *crater formation time* t_c. In units of t_0, it is thus $t_c = 38t_0$ (Ar) and $t_c = 71t_0$ (Cu).

The emission yield forms the only quantity where strong differences between the two systems are observed. For Ar, 158 atoms are emitted, roughly 15% of the crater volume ($V = 1072$); for Cu, in contrast, only 38 atoms are emitted, 6% of the crater volume ($V = 605$). Of these, 22 (58%) are reflected projectile atoms. This difference points at the fact that, in contrast to crater formation, sputtering is due to two different mechanisms: while gas flow contributes strongly in the sputtering of Ar,[57,58] for Cu the crater is excavated mainly by melt flow; these differences will be discussed in detail elsewhere. We note that in Ar we observed mostly sputtered monomers, and dimers contribute to less than 10%, while in Cu the number of dimers and larger emitted clusters is substantial, exceeding 50%.

B. Energy dependence of crater volumes

Figure 5 summarizes the energy dependence of the crater volumes induced by the smaller clusters simulated by us. Evidently the crater volumes for the two widely different

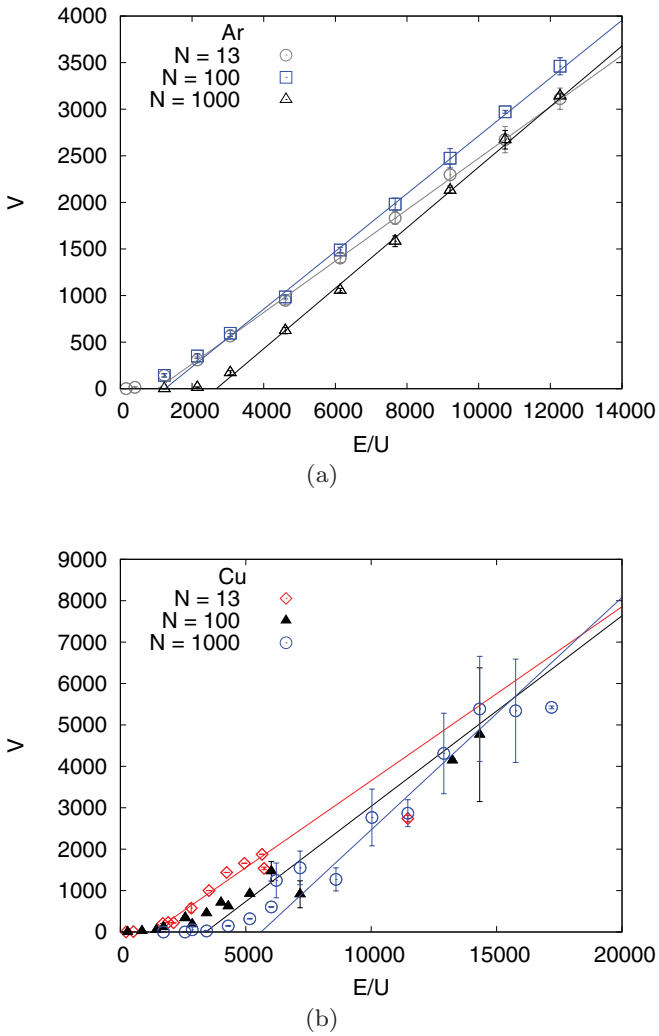

FIG. 5. (Color online) Crater volume V versus scaled energy $\epsilon = E/U$ for (a) Ar_N and (b) Cu_N clusters. Lines are linear fits [Eq. (6)]. The slopes, the *cratering efficiencies* are $a = 0.28$ (0.31, 0.325) for Ar clusters of size $N = 13$ (100, 1000) and $a = 0.42$ (0.46, 0.56) for Cu clusters.

materials, Ar and Cu, coincide rather well when the impact energy is scaled to the target cohesive energy $\epsilon = E/U$. The data are, to a good first approximation, well described by a linear law

$$V = a(\epsilon - \epsilon_c), \quad \epsilon > \epsilon_c \tag{6}$$

where the *cratering efficiency* $a \cong 0.3$, and ϵ_c is a threshold, which increases from $\epsilon_c = 1040$ ($N = 13$) over $\epsilon_c = 1240$ ($N = 100$) to 2680 ($N = 1000$) with the cluster size N. For Cu, it is $a \cong 0.4$–0.45, while the thresholds increase from 1300 over 3400 to 4400 for these sizes. For both targets, this increase follows a rough $N^{1/4}$ dependence (cf. Fig. 7 and the discussion in Sec. III C below). Aside from the threshold behavior and the roughly linear scaling, we note that craters in Cu tend to be somewhat larger than craters in Ar; we assume that this is due to the importance of the liquid phase in the metallic equation of state, which allows for effective mass transport (melt flow) out of the crater volume, thus widening them slightly more than in the case of Ar craters.

We rationalize the simple law [Eq. (6)] in which only one materials parameter, the cohesive energy U, describes the physics, as follows. Stopping proceeds rather quickly, on a time scale t_0 [Eq. (5)]. At this time, virtually all the cluster energy E is available close to the target surface for crater formation. The available energy can then be used for bond breaking in the target and hence atomize the material in the energized region, which is to become the crater volume. In agreement with the fact that only energies enter into the crater volume formula [Eq. (6)], arguments based on pressure and momentum play a minor role in the process.

We note that instead of the cohesive energy, one might as well introduce the critical temperature T_c of the liquid-gas transition into Eq. (6) if one wants to emphasize the thermophysical nature of the processes leading to crater formation. In fact, when temperatures $T > T_c$ are reached, the target material is completely gasified and free to flow out of the energized volume. However, kT_c and U are roughly proportional to each other, $kT_c = \alpha U$, where $\alpha \cong 0.15$ for a Lennard-Jones material like Ar, and $\alpha = 0.16$ for Cu.

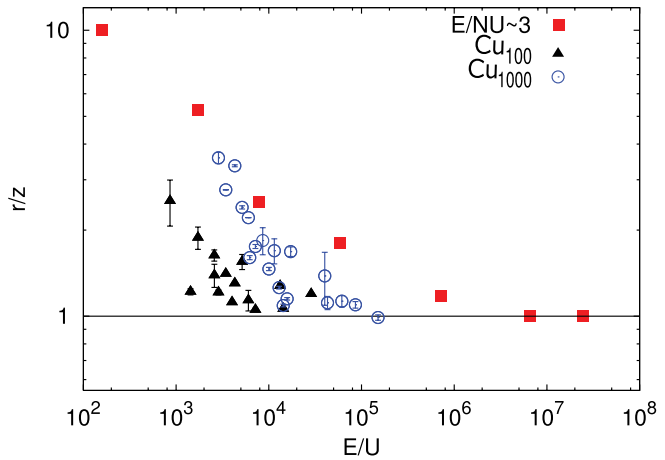

(a)

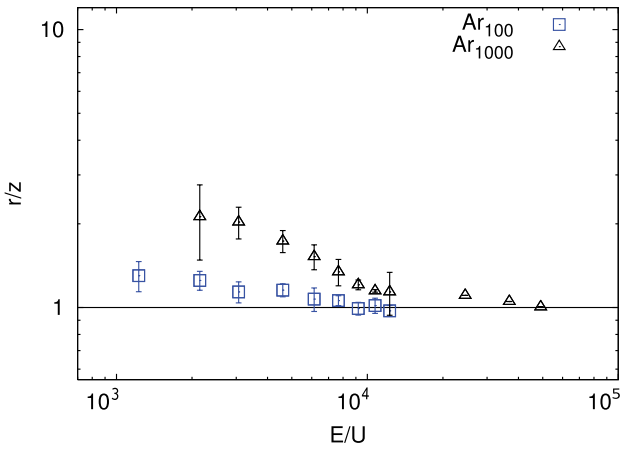

(b)

FIG. 6. (Color online) Crater aspect ratio r/z versus scaled energies $\epsilon = E/U$. (a) Cu data. Equivelocity data ($E/NU \sim 3$) (see Table I). (b) Ar data.

C. Crater shape

Figure 6 shows the aspect ratio r/z of the craters obtained in our simulations as a function of projectile energy and size. It is observed that, at low energies, craters are shallow, while they become hemispherical with increasing energy. The energy when hemisphericity is reached will be denoted by E_{hemi} in the following. This threshold energy E_{hemi} increases with increasing cluster size. Figure 7 analyzes this dependence quantitatively. Both for Ar and Cu clusters investigated, $N \leqslant 1000$, it is $E_{\text{hemi}} \propto N^{1/4}$. In Fig. 7, we include for comparison also the threshold energy E_{th} [which is identical to $U\epsilon_c$ in Eq. (6)], below which no crater is formed. It is seen that E_{hemi} is about a factor of 5 larger then E_{hemi}; that is, craters assume a hemispherical shape as soon as the impact energy is barely one order of magnitude above threshold to crater formation E_{th}.

The aspect ratios of the craters induced by the larger, equivelocity Cu clusters (Table I) have been included in Fig. 7. Since here $E/NU \cong$ const, the data increase in their energy E only because of increasing size N. Note that the second and third data points, with $N = 612$ and 2809, respectively (cf. Table I), agree nicely with our other results of Cu_{1000} impacts. For larger impact energy, and cluster size, the craters develop an increasingly hemispherical form. This is not in contradiction with our finding that E_{hemi} increases with cluster size N: since this increase is slow, $\propto N^{1/4}$, the energy per projectile atom $E_{\text{hemi}}/N \propto N^{-3/4}$ *decreases* with cluster size. At the same velocity, large clusters will excavate more hemispherically shaped craters, while small craters form shallow craters.

Crater shapes appear to have been measured experimentally, for mm-sized projectiles only; no data for μm-sized projectiles are known to us. In the latter case, usually only the crater radius is measured.[10,13,21,22] Murr *et al.*[4] discuss a wider variety of experimental data for mm-sized impactors; they investigate craters formed by Al, glass, and steel impactors in Al and Cu. In the hypervelocity regime, they find nearly hemispherical craters, both in experiment and in accompanying hydrocode

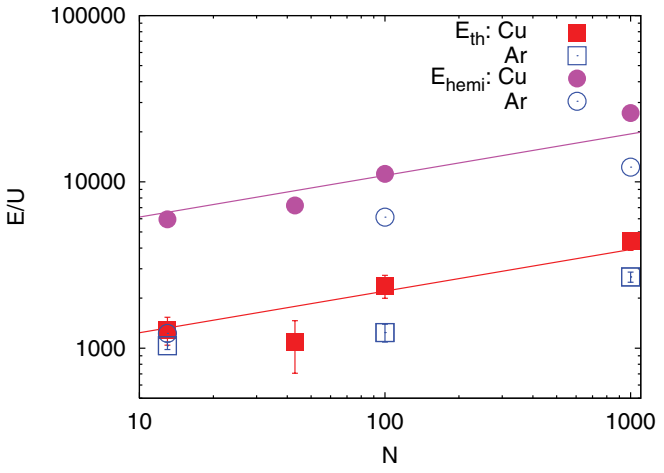

FIG. 7. (Color online) Dependence of threshold energies E_{th} and E_{hemi} on cluster size N. E_{th}: threshold for crater formation. E_{hemi}: threshold to hemispherical shape. Data for Cu_{13} and Cu_{43} clusters taken from Ref. 24. Lines show an $N^{1/4}$ dependence (see text).

simulations. They demonstrate that deviations from hemisphericity are linearly connected to $\sqrt{\rho_p/\rho_t}$, where $\rho_{p,t}$ is the mass density of the projectile and target, respectively. In his early study of iron impacts in a variety of metal targets, Rudolph[11] reports that in most target metals studied, with increasing projectile velocity craters become hemispherical; an exception is made by Al and Be targets, in which craters are deep, $r/z \cong 0.25$. Bernhard and Hörz[7] study cratering by 3.2-mm soda-lime glass impactors in Al; at high velocities, they find slightly deep craters, $r/z \cong 0.86$.

D. Correlation between emission yield and crater volume

While the crater is excavated, part of the crater material is sputtered. Figure 8 shows the correlation between emission yields Y and crater volumes V for Cu and Ar cluster impacts. We can roughly fit to a power law as

$$V = \beta Y^b. \tag{7}$$

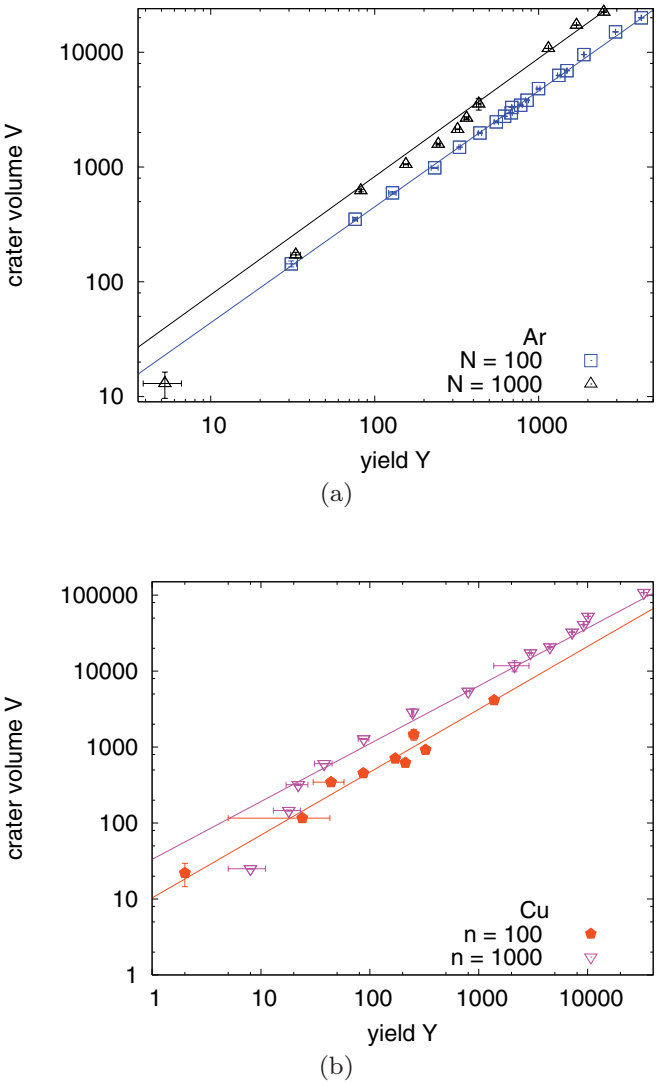

FIG. 8. (Color online) Correlation of emission yield Y with crater volume V for Ar (a) and Cu clusters (b). Lines showing correlation [Eq. (7)] to guide the eye.

For Ar craters, $b \cong 1$ (a least-squares fit to the data gives $b = 1.01 \pm 0.02$ for Ar_{100} and $b = 1.03 \pm 0.06$ for Ar_{1000}), and thus crater volumes and emission yields increase proportionally to each other with increasing cluster impact energy. Hence, for these targets, experimentally measured emission yields can be directly used to infer crater volumes (apart from a proportionality factor of ~4), and vice versa. We note that an analogous correlation holds for the sputter yield of target atoms; here, the exponents read as $b = 0.98 \pm 0.02$ for Ar_{100} and $b = 0.94 \pm 0.05$ for Ar_{1000}.

For Cu, the correlation between crater volumes and emission yields shows more scatter. A fit to Eq. (7) shows that the data follow a sublinear relationship with $b \cong 0.8$ ($b = 0.83 \pm 0.07$ for Cu_{100} and $b = 0.76 \pm 0.17$ for Cu_{1000}). Again, a restriction of the yield to the proper sputter yield of target atoms leads only to a small modification.

A simple proportionality, $b = 1$ in Eq. (7), indicates that sputtering contributes always in a similar fraction to crater excavation, in other words that the cratering mechanism does not depend on projectile energy (and cluster size). Other mechanisms (besides sputtering) which may contribute to crater excavation are the formation of the crater rim (see Figs. 1 and 2) and the compression of target material below the impactor. A superlinear behavior of V with Y ($b > 1$), as it is weakly seen for the highest impact energies for Ar impacts, indicates that for large projectile energies, sputtering contributes less to cratering. In the case of the weak Ar target, we assume that the high pressure induced by the projectile will dislocate atoms from the energized volume into the crater walls and the target inner; this compression will contribute to increasing V while leaving Y unchanged. A sublinear behavior ($b < 1$), as it is clearly observed for Cu impacts, indicates that slow projectiles form their craters with a relatively small contribution of sputtering. For metals, melt flow onto the surface is an important mechanism for crater formation, which proceeds without sputtering.

We assemble in Fig. 9 the ratio V/Y as a function of cluster size N. This plot shows the trends discussed above for the contribution of sputtering to crater formation. For Cu, sputtering contributes more to crater excavation than for Ar, in particular, for the larger cluster sizes. While for Cu we see

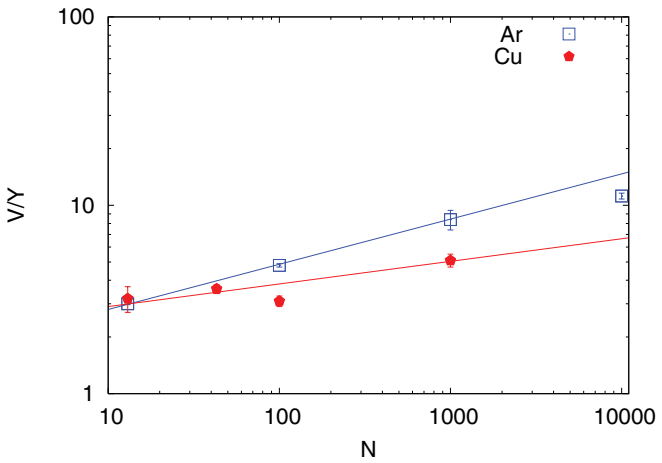

FIG. 9. (Color online) Ratio of crater volume V to emission yield Y as a function of cluster size N. Lines are to guide the eye.

only a mild dependence of V/Y with cluster size N, this ratio increases more strongly (like $N^{0.24}$) for Ar, indicating that for large Ar clusters, less than 10% of the excavated crater volume has been sputtered, while it is 30% for Ar_{13} impacts.

IV. DISCUSSION: EXTENSION TO LARGER PROJECTILE SIZES

A. Energy dependence of crater volumes: Big projectiles

It is excluded from a computational point of view to extend crater-formation simulation using molecular dynamics beyond a few tens nm projectile size. Indeed, the largest such simulation published up to now used a $D = 55$ nm Cu projectile containing $N = 7 \times 10^6$ atoms.[35] It is appropriate to compare our small-cluster cratering data in proportion to the bigger Cu cluster data simulated by us (Table I), and to experimentally available data. Such a comparison has been recently published,[35] with emphasis on the emergence of plastic flow for larger impactors. In the context of the present discussion, it is worthwhile to briefly summarize the main findings.

In the compilation Fig. 10(a), the experimental data have been taken from experiments with hypervelocity (0.8–23 km/s) metal particle impact on Cu. Both μm- and mm-sized projectiles have been included. References 4 and 14 report both crater depth and radius data for 3.18-mm-sized Fe and Al projectiles ($v \cong$ 1–6 km/s) impacting into Cu and allow for reliable crater volume determination via a half-ellipsoid approximation. References 21 and 22 present data of μm-sized Fe projectiles into a Cu target ($v \cong$ 5–25 km/s); here, only the crater diameter has been measured by secondary electron micrography; we determine the crater volumes by assuming a half-sphere geometry. These data are based on a reanalysis of previously published results. Note that these data show a dependence which is proportional to projectile velocity rather than to projectile energy. The data and their sources are summarized in Table II.

In Fig. 10, both the energies and the crater volumes plotted extend over more than 17 orders of magnitude. Lines following a linear law

$$V = a\epsilon \tag{8}$$

i.e., ignoring the threshold effect, have been included to guide the eye. As above, we call a the *cratering efficiency*. Three lines, one for the small cluster simulational data (Fig. 5) with $a = 0.28$, another for the μm-sized data ($a = 5.0$), and the third for mm-sized projectiles ($a = 23$). Evidently, a linear law describes the evolution of crater sizes with energy in a zeroth approximation quite well. However, the increase of the prefactor a demonstrates that large (high-energy) clusters make more efficient use of their energy for creating craters. Note that our simulational data with bigger Cu clusters coincide well with our previous results with smaller Cu clusters, as long as a crater is produced ($V > 1$). With increasing energy, they are more effective in crater production than the smaller clusters and exceed the estimate, Eq. (8), by a factor of 10 for the largest cluster. Thus, our big simulated cluster impacts bridge the gap between the nanoscopic craters of Fig. 5 and the micro- and macroscopic craters observed in experiment.

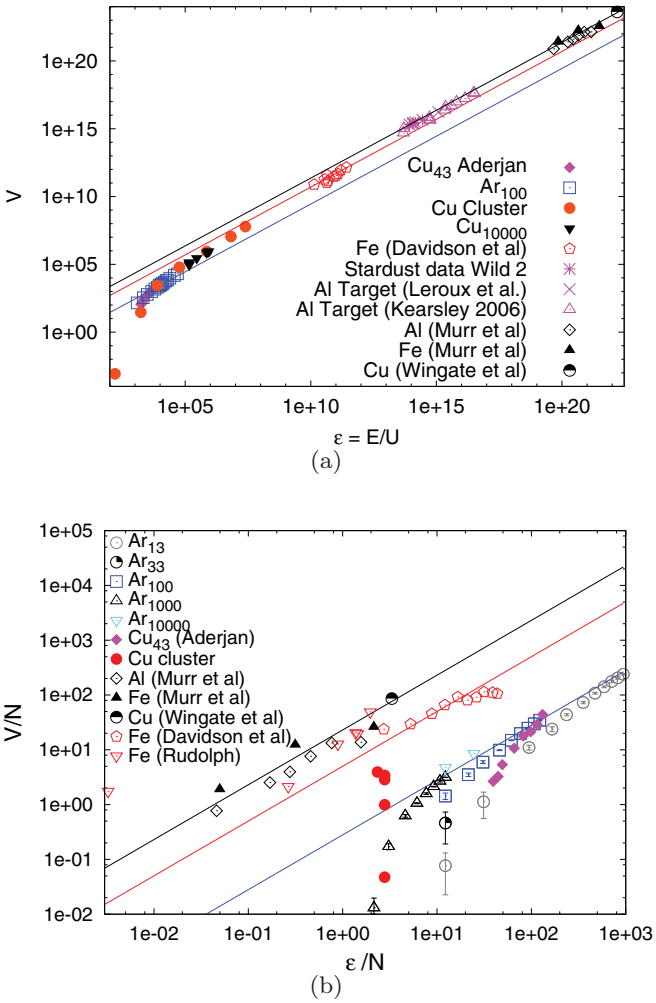

FIG. 10. (Color online) Synopsis of experimental and simulational data of crater volumes V vs scaled energies $\epsilon = E/U$ (a) and of reduced volumes V/N vs reduced scaled energies $\epsilon = E/UN$, (b) Legend indicates projectiles. Ar clusters (simulation results) impact onto an Ar target, while all other data are on cratering of a Cu target. The data by Aderjan *et al.* (Ref. 24) and of Cu cluster impact (cf. Table I) are simulation results. The remaining data are experimental results obtained by Murr *et al.* (Ref. 4), Wingate *et al.* (Ref. 20), Davidson *et al.* (Ref. 21), and Rudolph (Ref. 11) (cf. Table II). Lines indicate a linear relationship, Eq. (8), and have been fitted to the data of mm-sized projectiles (by Murr *et al.* and Wingate), to the data of μm-sized projectiles (Davidson *et al.*), and to the Ar_{100} data, respectively. Lines in figures (a) and (b) are identical. Data partly taken from Ref. 35.

We note that it is possible to fit a law $V = a\epsilon^{\gamma}$, through the set of data displayed between $\epsilon = 10^3$ and 10^{21}, where $\gamma = 1.1$. However, we see no physical justification for such a purely empirical fit, and rather want to introduce the idea that cluster size N becomes an important second parameter to describe the cratering data.

Figure 10(b) shows the same data reduced to the number N of projectiles. Here, we also include experimental data by Rudolph[11] of μm-sized Fe projectiles impacting Cu ($v \cong$ 0.5−5 km/s); since here no absolute energies and crater volumes are available, these data could not be incorporated into Fig. 10(a). Note that due to the considerable scatter in

TABLE II. Cratering data of selected experiments on Cu targets bombarded by μm- and mm-sized metal projectiles. Data not presented in Ref. 11 are indicated by a dash (–). Data partly taken from Ref. 35.

Projectile	N	v (km/s)	E/U	E/NU	V	V/N	Ref.
Cu	4.8×10^{21}	6.0	1.6×10^{22}	3.3	4.1×10^{23}	85.39	20
Al	1.0×10^{21}	1.08	4.7×10^{19}	0.05	7.8×10^{20}	0.77	14
		2.07	1.7×10^{20}	0.17	2.6×10^{21}	2.52	
		2.64	2.8×10^{20}	0.28	4.0×10^{21}	3.95	
		3.40	4.6×10^{20}	0.46	7.7×10^{21}	7.60	
		4.40	7.7×10^{20}	0.76	1.3×10^{22}	13.29	
		6.01	1.5×10^{21}	1.43	1.4×10^{22}	13.71	
Fe	1.42×10^{21}	0.78	7.1×10^{19}	0.05	2.6×10^{21}	1.86	4
		1.96	4.5×10^{20}	0.31	1.8×10^{22}	12.34	
		5.12	3.1×10^{21}	2.15	3.7×10^{22}	26.12	
Fe	1.63×10^{10}	5.77	4.43×10^{10}	2.72	3.84×10^{11}	23.7	21
	2.60×10^{9}	8.01	1.36×10^{10}	5.24	7.62×10^{10}	29.5	
	4.05×10^{9}	10.39	3.57×10^{10}	8.82	1.83×10^{11}	45.5	
	2.15×10^{10}	12.17	2.60×10^{11}	12.09	1.41×10^{12}	65.8	
	9.46×10^{9}	14.24	1.57×10^{11}	16.57	8.63×10^{11}	91.6	
	5.78×10^{9}	16.03	1.21×10^{11}	21.00	4.62×10^{11}	80.5	
	3.93×10^{9}	17.88	1.03×10^{11}	26.13	3.57×10^{11}	91.1	
	2.65×10^{9}	19.63	8.34×10^{10}	31.48	2.99×10^{11}	113.4	
	1.27×10^{9}	21.81	4.92×10^{10}	38.86	1.39×10^{11}	110.6	
	9.89×10^{8}	23.04	4.29×10^{10}	43.37	1.04×10^{11}	105.9	
Fe	–	1.08	–	0.0033	–	1.75	11
	–	2.04	–	0.26	–	2.14	
	–	3.71	–	0.89	–	12.8	
	–	5.30	–	1.44	–	19.7	
	–	5.09	–	1.37	–	20.5	
	–	7.00	–	1.96	–	49.2	
Comet	8.83×10^{13}	6.1	1.21×10^{14}	1.37	2.66×10^{15}	30.09	59
	6.83×10^{13}		8.64×10^{13}	1.27	2.03×10^{15}	29.67	
	7.86×10^{13}		1.11×10^{14}	1.41	2.37×10^{15}	30.10	
	1.96×10^{14}		2.83×10^{14}	1.45	4.46×10^{15}	22.76	
	9.68×10^{13}		1.45×10^{14}	1.50	2.96×10^{15}	30.55	
Glass	1.05×10^{15}	6.02	1.20×10^{15}	1.14	1.69×10^{16}	16.06	60
Glass	3.69×10^{13}	5.93	4.11×10^{13}	1.11	4.58×10^{14}	12.40	61
	3.69×10^{13}	6.06	4.29×10^{13}	1.16	9.95×10^{14}	26.93	
	4.06×10^{14}	5.97	4.57×10^{14}	1.13	4.09×10^{15}	10.08	
	4.06×10^{14}	5.92	4.49×10^{14}	1.11	6.50×10^{15}	16.03	
	4.06×10^{14}	6.12	4.80×10^{14}	1.18	4.05×10^{15}	10.00	
	1.62×10^{15}	6.05	1.88×10^{15}	1.16	2.19×10^{16}	13.52	
	1.62×10^{15}	6.21	1.98×10^{15}	1.22	3.91×10^{16}	24.12	
	2.93×10^{15}	6.09	3.44×10^{15}	1.17	4.69×10^{16}	15.97	
	4.64×10^{15}	6.03	5.34×10^{15}	1.15	8.97×10^{16}	19.32	
	1.02×10^{16}	6.05	1.18×10^{16}	1.16	1.62×10^{17}	15.87	
	2.31×10^{16}	6.22	2.83×10^{16}	1.22	3.63×10^{17}	15.71	
	2.31×10^{16}	5.96	2.60×10^{16}	1.12	4.29×10^{17}	18.57	

these data, they have not been used for the fitting; if included, the cratering efficiency would have risen to $a = 11 \pm 10$, while in the other cases the uncertainty in a is only of the order of $\pm 10\%$. Several effects are noteworthy:

(i) The nanoscopic crater data obtained by simulation (see Fig. 5) assemble quite well on one line. Due to the threshold effect, for each fixed cluster size, the data deviate from the line at the low-energy end of the fit line.

(ii) Both the experimental data for μm- and mm-sized projectiles align well on linear fit lines [Eq. (8)]. The μm-sized data show a larger scatter than the other data sets.

(iii) The mm-sized data have a higher cratering efficiency than the μm-sized (and the simulational) data.

(iv) The threshold energy E_{th} is not particularly sensitive on the projectile size N. As a consequence, small cluster need high specific energies ϵ/N to reach the linear law, while for large clusters, the linear law extends down to small values of ϵ/N. As a consequence, the threshold effect becomes unobservable for large projectile impact and hence the experimental data.

(v) We performed simulations for Ar projectiles of fixed specific energy $\epsilon/N = 12$ and varying size ($N = 13$–10^4). Here, the small clusters are close to the threshold energy (with

correspondingly reduced crater volumes), while the specific crater volume V/N for large clusters ($N \geqslant 100$) has saturated.

(vi) A further set of simulations has been performed for equivelocity Cu clusters impinging on Cu (Table I). Again, large clusters create larger specific volumes V/N, which is explained by the same threshold effect as the item above. Indeed, for the largest impacts, V/N appears to saturate. But, note that the saturation value is considerably above the fit line, Eq. (6), describing the other simulational data. Indeed, these simulational data approach the data and the line describing μm-sized projectiles.

B. Cratering times

A suitable time scale for the time t_c it takes to form a crater is provided by the time t_0 for the projectile to move a distance equal to its diameter D at the initial impact velocity v [Eq. (5)]. In fact, recent simulation results show that the maximum stopping and deformation of impacting Cu clusters occurs roughly at $\sim 0.5t_0$.[53]

The actual time for crater formation is more than one order of magnitude longer due to (i) the slowing down of the projectile, (ii) the time the excavation process takes, and (iii) the time needed for the final settling of the crater volume. In fact, in Sec. III A we found that for the special case of clusters containing $N = 1000$ atoms and impacting at a specific energy of $\epsilon/N = 6.1$ that $t_c = 38t_0$ (Ar) and $t_c = 71t_0$ (Cu).

For macroscopic craters, this time may be even longer. Walsh *et al.*[62] estimate the crater formation time as

$$t_c = wt_0, \tag{9}$$

where the factor w is given by

$$w = 3.87\left(\frac{\rho v^2}{Y}\right)^{0.282}. \tag{10}$$

This assumes that plastic flow is relevant for crater formation for a material of yield strength Y and density ρ.

Evolution of cratering time t_c with projectile size N is, therefore, mainly due to the $N^{1/3}$ dependence of t_0. There is a slight contribution due to Y, because Y depends on the strain rate η,[48] and η depends on $N^{1/3}$ as discussed in Ref. 34.

Let us specialize on Cu impacts on a Cu target (density $\rho = 8.94 \times 10^3$ kg/m^3) with a velocity $v = 5$ km/s. If we use the typical yield strength of single-crystalline Cu, $Y \sim 0.1$ GPa, we obtain a factor $w_{0.1} = 34$. However, for nanoimpactors one should use the yield strength of single-crystalline Cu at high strain rates, which is $Y \sim 1$ GPa;[48] then $w_1 = 18$.

In a recent publication,[35] data were presented for crater formation induced by a $D = 20$ nm impactor at $v = 5$ km/s ($t_0 = 4$ ps) into a Cu target. The MD cratering time amounted to $t_c \sim 20$ ps. For this impact, certainly the high-strain-rate value $w_1 = 18$ needs to be used, such that Eq. (9) predicts with $t_0 = 4$ ps, $t_c = 72$ ps, which is a factor 3.6 larger than the MD result. Considering all the simplifications used in the macroscopic estimate equation (9), this is a good estimate for the times observed in MD. Walsh *et al.* [Eq. (9)] overestimate the nanoscopic cratering time because plastic flow is slower than liquid flow and sputtering/evaporation, which also contribute for nanoclusters.

As projectile size increases beyond the nanoscale, cratering times become longer, matching Eq. (9), due to the increasing contribution of plastic flow. Plastic flow becomes possible as soon as dislocations are generated in the target; these start moving due to the stress gradients existing after projectile impact and transport matter away from the impact zone. However, we note that, for projectile sizes below a few nm, plastic flow is no longer meaningful to define cratering times as assumed in Eq. (9) because the projectile disintegrates in $\sim 0.5t_0$, which would be shorter than typical phonon periods ($\sim$1 ps), and there is no contribution from dislocation activity.

Dislocation densities can readily be detected from molecular-dynamics simulations. These densities can be directly related to experimental hardness measurements below an impact crater. An example of such a comparison was presented in the Supplemental Material of Ref. 35.

C. Strain rate

We have recently published results[53] on the strain rates occurring for nanometer-sized cluster impacts. They can be summarized as follows. Strain rate η depends on projectile size as $\eta = 0.5/t_0$, where t_0 is given above [Eq. (5)]. This result corresponds to strain rates of the order $\eta = 10^5$ s^{-1} for cm-sized projectiles, which agrees with continuum level simulations and models. However, the resulting large increase of several orders of magnitude in strain rate as one goes from macroscopic to nanoscopic impacts would only increase yield strength by one order of magnitude, and this is not enough to explain discrepancies in crater size, as shown by previous hydrocode simulations[4,14] and discussed in the main text. In summary, we argue that the value $\eta = 0.5/t_0$ gives a satisfactory approximation for the strain rates occurring under cluster impact.

D. Ductile versus brittle behavior

In this work, we find that crater formation by cluster impact proceeds in an astonishingly similar way for metallic (Cu) and van der Waals–bonded targets (Ar). These two materials may be considered as prototypical for ductile and brittle materials, respectively. Indeed, for decades, simulations of brittle and ductile solids have been carried out using respectively Lennard-Jones (LJ) and embedded atom method (EAM) interaction potentials.[63–65] Continuing with that tradition, we recently presented a study on both LJ Ar and EAM Cu, focusing on smaller clusters, showing similar behavior in the stopping and strain rates produced by such impacts.[53] For larger projectiles, brittle solids might fragment more readily, especially in the presence of pre-existing defects.

Brittle fracture will facilitate the removal of large chunks of materials at a low energetic cost. On the other hand, plastic flow will be likely reduced due to large strength and low dislocation mobilities in such materials. Melt flow will also be reduced due to the large melting temperature of brittle materials, which are usually refractory. As a result, cratering efficiency is not affected for nanoscale projectiles significantly compared to ductile materials, and it might not be affected at larger projectile dimensions, and similar scaling issues going from nano to macro would be expected.

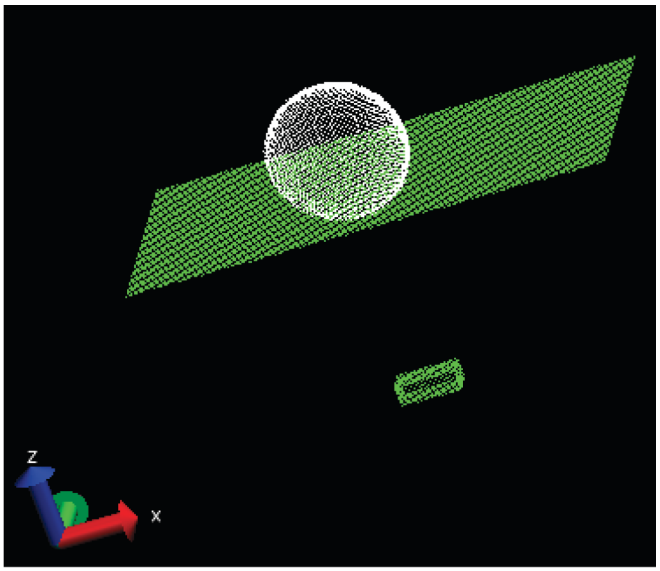

(a)

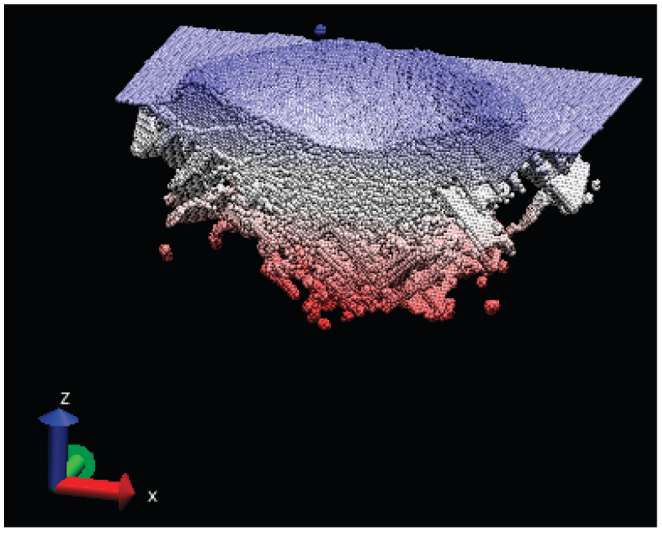

(b)

FIG. 11. (Color online) Snapshots of a cratering simulation for a target with a crack. Only defective (non-fcc) atoms filtered with a centrosymmetry parameter (Ref. 67) are shown for one half of the sample. (a) Initial configuration, showing surfaces and the crack below the impact point. (b) Crater 27 ps after impact, showing a layer of molten material and a thick region with an immense dislocation density, which destroys any evidence of the crack. Color scale indicates depth.

Recently, cratering simulations were performed on silica.[30] Impact by 20–40 km/s Ar clusters containing $\sim 10^5$ atoms on thin films led to sizable cratering accompanied by fracture *below* the impact point.[66]

Cratering efficiency a in the macro regime will be strongly affected by pre-existing microstructure of the sample, such as dislocation sources, grain boundaries, cracks, etc., all of which might increase a, by easing plastic flow and the ejection of large fragments without the need to break bonds, as in brittle fracture mentioned above.

In an attempt to investigate whether cratering of ductile materials is affected by pre-existing damage inside the material, we proceeded as follows. We performed cratering simulations as described before, using the Cu potential developed by Mishin.[40] Target size was $100 \times 100 \times 100$ fcc cells, with Langevin damping at the sides and bottom surfaces. Projectile had 5 nm radius and 5 km/s impact velocity. We used a variable time-step scheme to guarantee energy conservation. A thin nanocrack was introduced in the target to study if the collapse of the crack might increase crater volume. The crack was created by removing atoms from a prismatic box, sized $4 \times 4 \times 1.1\ \mathrm{nm}^3$, at a depth of 12 nm below the impact point, as can be seen in Fig. 11(a). Such nanocracks could be produced by a number of reasons, including accumulation of radiation damage, pre-existing mechanical deformation, etc. The target with the crack was relaxed before the impact. Figure 11(b) shows that 27 ps after impact the crack has been obliterated by plastic flow. Additional simulations (not shown here) show that cracks positioned higher are destroyed by the molten flow. The crater volume, approximated by an ellipsoid, is actually $\sim 6\%$ smaller for the case with the crack than for the same target without a crack. Variations in crater volume smaller than 10% can not be considered statistically significant in our simulations. We can therefore conclude that nano-sized defects might not play a critical role in crater volume in ductile solids. However, the situation might be different in brittle materials. As mentioned above, silica shows fracture under impact,[66] and thus pre-existing cracks might help projectile penetration in brittle solids.

V. CONCLUSIONS

Using molecular-dynamics simulation, we study the crater volumes induced by hypervelocity impacts ($v = 3$–100 km/s) of projectiles containing up to $N = 10^6$ atoms. We find the following:

(i) Above a threshold E_{th}, the crater volume V increases linearly with the total cluster energy E. Thus, it is not the velocity nor the size of the cluster alone which determine the crater volume, but rather a single parameter E.

(ii) The crater volume is, to a good approximation, independent of the target material if the impact energy E is scaled to the target cohesive energy U. This conclusion is based on self-bombardment of a van der Waals–bonded and a metallic material; it needs further confirmation for other materials.

(iii) The threshold energy increases slowly, like $N^{1/4}$, with cluster size N.

(iv) At threshold, craters are shallow. They become hemispheric at energies $\sim 5E_{\mathrm{th}}$.

(v) Part of the material excavated from the crater is sputtered. This fraction decreases with cluster size N. Relatively less material is sputtered from an Ar target than from a Cu target.

(vi) Simulations with larger projectiles (up to $N = 10^6$) show a systematic deviation from the conclusion (i) above: the crater volume increases slightly more than linearly with cluster energy E.

(vii) This finding is in agreement with available experimental data on cratering by μm- and mm-sized projectiles, which

exhibit a higher cratering efficiency. Quantitatively, the cratering efficiency a rises from $a = 0.29$ for nm-sized projectiles, over $a = 5.0$ for μm-sized data (experiment), to a value of $a = 23$ for mm-sized projectiles.

(viii) Simulations on predamaged samples containing nanocracks show that these pre-existing defects play only a negligible role for crater formation and size in metals.

Part of these conclusions [(i), (ii), (vi), and (vii)] have already been drawn, using a less systematic basis of MD simulations, in previous work,[34,35] but are corroborated by the present, more extended set of simulations.

ACKNOWLEDGMENT

E.M.B. and F.F. would like to thank a grant from the SeCTyP U. N. Cuyo, and Grant No. PICT2009-0092 from the Argentinean Agencia Nacional de Promoción Científica y Tecnológica.

*urbassek@rhrk.uni-kl.de

[1] R. E. Johnson, *Energetic Charged-Particle Interactions with Atmospheres and Surfaces* (Springer, Berlin, 1990).
[2] B. T. Draine, Annu. Rev. Astron. Astrophys. **41**, 241 (2003).
[3] J. R. Baker, Int. J. Impact Eng. **17**, 25 (1995).
[4] L. E. Murr, S. A. Quinones, E. Ferreyra, A. Ayala, O. L. Valerio, F. Hörz, and R. P. Bernhard, Mater. Sci. Eng. A **256**, 166 (1998).
[5] J. L. Warren, H. A. Zook, J. H. Alton, U. S. Clanton, C. B. Dardano, J. A. Holder, R. R. Marlow, R. A. Schultz, L. A. Watts, and S. J. Westworth, *Proceedings of the 19th Lunar Planetary Science Conference* (Lunar and Planetary Institute, Houston, 1989), p. 641.
[6] R. P. Bernhard, T. H. See, and F. Hörz, in *LDEF 69 Months in Space–2nd Post-Retrieval Symposium*, Vol. 3194 of NASA Conference Proceedings, Part 2, edited by A. S. Levine (NASA Langley Research Center, Hampton, VA, 1993), p. 551.
[7] R. P. Bernhard and F. Hörz, Int. J. Impact Eng. **17**, 69 (1995).
[8] N. Altobelli, S. Kempf, M. Landgraf, R. Srama, V. Dikarev, H. Krüger, G. Moragas-Klostermeyer, and E. Grün, J. Geophys. Res. **108**, 8032 (2003).
[9] F. Hörz, R. Bastien, J. Borg, J. P. Bradley, J. C. Bridges, D. E. Brownlee, M. J. Burchell, M. Chi, M. J. Cintala, Z. R. Dai *et al.*, Science **314**, 1716 (2006).
[10] G. A. Graham, N. McBride, A. T. Kearsley, G. Drolshagen, S. F. Green, J. A. M. McDonnell, M. M. Grady, and I. P. Wright, Int. J. Impact Eng. **26**, 263 (2001).
[11] V. Rudolph, Z. Naturforsch. A **24**, 326 (1969).
[12] K. Eichhorn and E. Grün, Planet. Space Sci. **41**, 429 (1993).
[13] G. L. Stradling, G. C. Idzorek, B. P. Shafer, H. L. Curling Jr., M. T. Collopy, A. A. H. Blossom, and S. Fuerstenau, Int. J. Impact Eng. **14**, 719 (1993).
[14] S. A. Quinones and L. E. Murr, Phys. Status Solidi A **166**, 763 (1998).
[15] S. E. Donnelly and R. C. Birtcher, Phys. Rev. B **56**, 13599 (1997).
[16] R. C. Birtcher, J. Matsuo, and I.Yamada, Nucl. Instrum. Methods Phys. Res., Sect. B **175-177**, 36 (2001).
[17] H. J. Melosh, *Impact Cratering: A Geologic Process* (Oxford University Press, New York, 1989).
[18] K. A. Holsapple and R. M. Schmidt, J. Geophys. Res. **92**, 6350 (1987).
[19] K. A. Holsapple, Annu. Rev. Earth Planet Sci. **21**, 333 (1993).
[20] C. A. Wingate, R. F. Stellingwerf, R. F. Davidson, and M. W. Burkett, Int. J. Impact Eng. **14**, 819 (1993).
[21] R. F. Davidson and M. L.Walsh, AIP Conf. Proc. **370**, 1159 (1996).
[22] R. F. Davidson, Los Alamos National Laboratory Memorandum ESA-EA:95-248, 1995 (unpublished).
[23] D. L. Preston, D. L. Tonks, and D. C. Wallace, J. Appl. Phys. **93**, 211 (2003).
[24] R. Aderjan and H. M. Urbassek, Nucl. Instrum. Methods Phys. Res., Sect. B **164-165**, 697 (2000).
[25] T. J. Colla, R. Aderjan, R. Kissel, and H. M. Urbassek, Phys. Rev. B **62**, 8487 (2000).
[26] E. M. Bringa, K. Nordlund, and J. Keinonen, Phys. Rev. B **64**, 235426 (2001).
[27] K. Nordlund, Phys. World **14**, 22 (2001).
[28] J. Samela and K. Nordlund, Phys. Rev. Lett. **101**, 027601 (2008).
[29] T. Aoki, T. Seki, S. Ninomiya, K. Ichiki, and J. Matsuo, Nucl. Instrum. Methods Phys. Res., Sect. B **267**, 1424 (2009).
[30] J. Samela and K. Nordlund, Phys. Rev. B **81**, 054108 (2010).
[31] H. M. Urbassek, in *Sputtering by Particle Bombardment*, edited by R. Behrisch and W. Eckstein, Vol. 110 (Springer, Berlin, 2007), pp. 189–230.
[32] J. Samela and K. Nordlund, Nucl. Instrum. Methods Phys. Res., Sect. B **267**, 2980 (2009).
[33] A. Delcorte and B. J. Garrison, J. Phys. Chem. C **111**, 15312 (2007).
[34] C. Anders, G. Ziegenhain, S. Zimmermann, and H. M. Urbassek, Nucl. Instrum. Methods Phys. Res., Sect. B **267**, 3122 (2009).
[35] C. Anders, E. M. Bringa, G. Ziegenhain, G. A. Graham, J. F. Hansen, N. Park, N. E. Teslich, and H. M. Urbassek, Phys. Rev. Lett. **108**, 027601 (2012).
[36] C. Anders, H. M. Urbassek, and R. E. Johnson, Phys. Rev. B **70**, 155404 (2004).
[37] A. Michels, H. Wijker, and H. K. Wijker, Physica (Amsterdam) **15**, 627 (1949).
[38] J.-P. Hansen and L. Verlet, Phys. Rev. **184**, 151 (1969).
[39] M. S. Daw, S. M. Foiles, and M. Baskes, Mater. Sci. Rep. **9**, 251 (1993).
[40] Y. Mishin, D. Farkas, M. J. Mehl, and D. A. Papaconstantopoulos, Phys. Rev. B **59**, 3393 (1999).
[41] W. D. Wilson, L. G. Haggmark, and J. P. Biersack, Phys. Rev. B **15**, 2458 (1977).
[42] J. F. Ziegler, J. P. Biersack, and U. Littmark, *The Stopping and Range of Ions in Solids* (Pergamon, New York, 1985).
[43] E. M. Bringa, J. U. Cazamias, P. Erhart, J. Stölken, N. Tanushev, B. D. Wirth, R. E. Rudd, and M. J. Caturla, J. Appl. Phys. **96**, 3793 (2004).
[44] B. L. Holian and P. S. Lomdahl, Science **280**, 2085 (1998).
[45] T. C. Germann, B. L. Holian, P. S. Lomdahl, and R. Ravelo, Phys. Rev. Lett. **84**, 5351 (2000).
[46] Y. Mishin, M. J. Mehl, D. A. Papaconstantopoulos, A. F. Voter, and J. D. Kress, Phys. Rev. B **63**, 224106 (2001).

[47]P. Brüesch, *Phonons: Theory and Experiments I*, Vol. 34 of Springer Series of Solid-State Science (Springer, Berlin, 1982).

[48]W. J. Murphy, A. Higginbotham, G. Kimminau, B. Barbrel, E. M. Bringa, J. Hawreliak, R. Kodama, M. Koenig, W. McBarron, M. A. Meyers *et al*., J. Phys.: Condens. Matter **22**, 065404 (2010).

[49]L. Zheng, Q. An, Y. Xie, Z. Sun, and S.-N. Luo, J. Chem. Phys. **127**, 164503 (2007).

[50]E. M. Bringa and R. E. Johnson, Nucl. Instrum. Methods Phys. Res., Sect. B **143**, 513 (1998).

[51]See Supplemental Material at http://link.aps.org/supplemental/10.1103/PhysRevB.85.235440 for a computer animation of the impact event shown in Fig. 3.

[52]T. J. Colla and H. M. Urbassek, Radiat. Eff. Defects Solids **142**, 439 (1997).

[53]C. Anders, E. M. Bringa, G. Ziegenhain, and H. M. Urbassek, New J. Phys. **13**, 113019 (2011).

[54]S. D. Stoddard, J. Comput. Phys. **27**, 291 (1978).

[55]R. K. Crawford, in *Rare Gas Solids III*, edited by M. L. Klein and J. A. Venables (Academic, London, 1977), p. 663.

[56]A. V. Bushman, G. I. Kanel', A. L. Ni, and V. E. Fortov, *Intense Dynamic Loading of Condensed Matter* (Taylor & Francis, Washington, DC, 1993), first edition published in 1988 by the Institute of Chemical Physics, USSR Academy of Sciences.

[57]H. M. Urbassek and J. Michl, Nucl. Instrum. Methods Phys. Res., Sect. B **22**, 480 (1987).

[58]H. M. Urbassek and K. T. Waldeer, Phys. Rev. Lett. **67**, 105 (1991).

[59]A. T. Kearsley, J. Borg, G. A. Graham, M. J. Burchell, M. J. Cole, H. Leroux, J. C. Bridges, F. Hörz, P. J. Wozniakiewicz, P. A. Bland *et al*., Meteorit. Planet. Sci. **43**, 41 (2008).

[60]H. Leroux, J. Borg, D. Troadec, Z. Djouadi, and F. Hörz, Meteorit. Planet. Sci. **41**, 181 (2006).

[61]A. T. Kearsley, M. J. Burchell, F. Hörz, M. J. Cole,, and C. S. Schwandt, Meteorit. Planet. Sci. **41**, 167 (2006).

[62]J. M. Walsh, G. L. Stradling, G. C. Idzorek, B. P. Shafer, and H. L. Curling Jr., Int. J. Impact Eng. **14**, 775 (1993).

[63]B. L. Holian, A. F. Voter, N. J. Wagner, R. J. Ravelo, S. P. Chen, W. G. Hoover, C. G. Hoover, J. E. Hammerberg, and T. D. Dontje, Phys. Rev. A **43**, 2655 (1991).

[64]N. J. Wagner, B. L. Holian, and A. F. Voter, Phys. Rev. A **45**, 8457 (1992).

[65]S. J. Zhou, D. M. Beazley, P. S. Lomdahl, and B. L. Holian, Phys. Rev. Lett. **78**, 479 (1997).

[66]E. Holmström, J. Samela, and K. Nordlund, Europhys. Lett. **96**, 16005 (2011).

[67]C. L. Kelchner, S. J. Plimpton, and J. C. Hamilton, Phys. Rev. B **58**, 11085 (1998).